Numerical investigation of coastal circulation dynamics near Cape Hatteras, North Carolina, in January 2005

Yanlin Gong · Ruoying He · Glen G. Gawarkiewicz · Dana K. Savidge

Abstract A realistic regional ocean model is used to hindcast and diagnose coastal circulation variability near Cape Hatteras, North Carolina, in January 2005. Strong extratropical winter storms passed through the area during the second half of the month (January 15–31), leading to significantly different circulation conditions compared to those during the first half of the month (January 1–14). Model results were validated against sea level, temperature, salinity, and velocity observations. Analyses of along-shelf and cross-shelf transport, momentum, and kinetic energy balances were further performed to investigate circulation dynamics near Cape Hatteras. Our results show that during the strong winter storm period, both along-shelf (southward) and cross-shelf (seaward) transport increased significantly, mainly due to increases in geostrophic velocity associated with coastal sea level setup. In terms of momentum balance, the wind stress was mainly balanced by bottom friction. During the first half of month, the dominant kinetic energy (KE) balance on the shelf was between the time rate of KE change and the pressure work, whereas during the stormy second half of month, the main shelf KE balance was achieved between wind stress work and dissipation.

Y. Gong · R. He (✉)
Department of Marine, Earth and Atmospheric Sciences, North Carolina State University, Raleigh, NC, USA
e-mail: rhe@ncsu.edu

G. G. Gawarkiewicz
Department of Physical Oceanography, Woods Hole Oceanographic Institution, Woods Hole, MA, USA

D. K. Savidge
Skidaway Institute of Oceanography, Savannah, GA, USA

1 Introduction

Located on the east coast of North Carolina, USA, Cape Hatteras separates two oceanographically different regions: the Middle Atlantic Bight (MAB) and the South Atlantic Bight (SAB) (Fig. 1). The southwestward mean MAB shelf flow and northeastward mean SAB shelf flow converge off Cape Hatteras. At the same time, the Gulf Stream travels through the area and separates from the continental slope near Cape Hatteras.

While MAB shelf waters make occasional excursions into the SAB, much of its transport is diverted offshore and entrained into the Gulf Stream (Ford 1952; Fisher 1972; Kupferman and Garfield 1977; Gawarkiewicz et al. 2009). Churchill and Berger (1998), for example, examined the processes of MAB shelf water entrainment into the Gulf Stream and identified two export areas. The MAB shelf water export in the northern zone (35.4° N–36.1° N) was due to seaward movement of shelf water into Gulf Stream meanders. The shelf water export in the southern zone (35.2° N–35.4° N) was associated with seaward flow of shelf water in a strong current (5–10 cm/s) at the edge of the Hatteras Front. The warm salty shelf water in the SAB has a mean northward transport and was also exported into open-ocean near Cape Hatteras (Lee et al. 1991; Savidge and Bane 2001). Savidge and Savidge (2014) found that the magnitude of year-round SAB shelf water export at Cape Hatteras was as large as the exported MAB shelf water, with large seasonal variability.

Strong meteorological forcing, such as winter extratropical storms, also has significant impact on Cape Hatteras circulation and its export process. Extensive observational studies, such as the Genesis of Atlantic Lows Experiment (GALE)
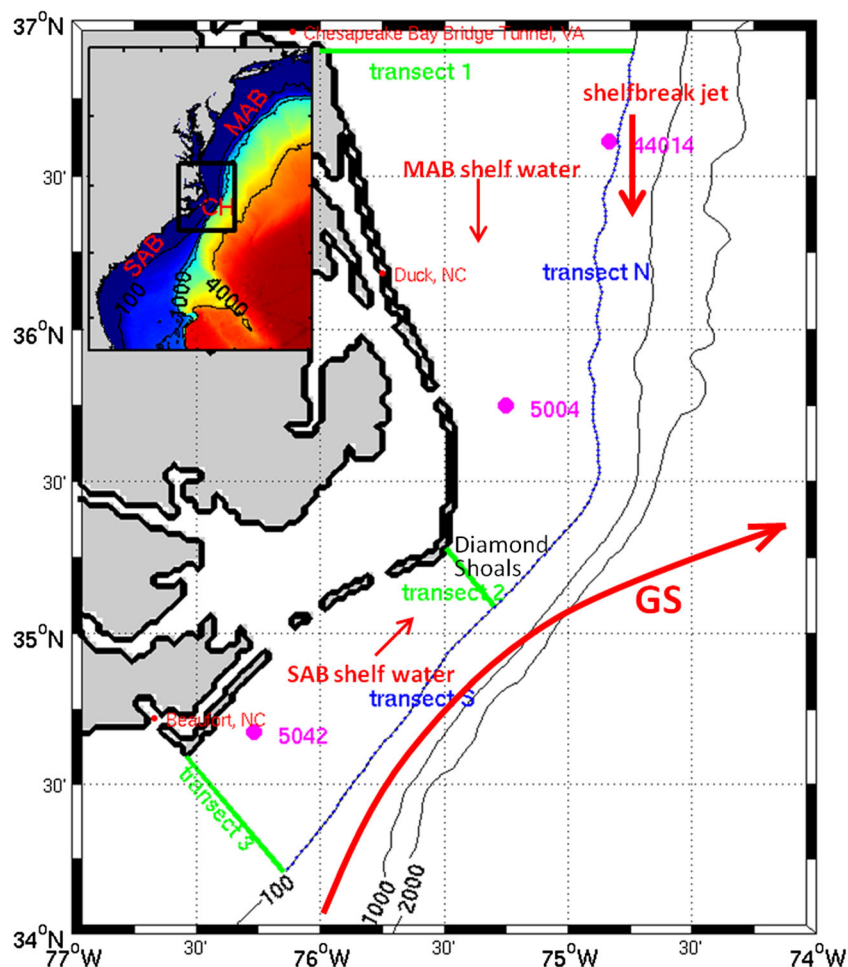
Fig. 1 Cape Hatteras study
region (*main frame and black box
in inset*) and MABSAB
circulation model domain and
bathymetry (*inset*). Schematic of
main currents in this region is
shown in the main frame, along
with location of tidal gauge
stations, across-shelf transects (1–
3), and along-shelf transects (N,
S) and locations of NDBC buoy
44014 and ADCP moorings
(5004 and 5042)

(Dirks et al. 1988), have been conducted to study the marine boundary layer dynamics and air-sea interactions associated with extratropical cyclone formation in this region. Further, two-dimensional (Chao 1992; Xue et al. 2000) and three-dimensional (Li et al. 2002; Nelson and He 2012) atmosphere-ocean coupled models were used to understand the development of the atmospheric mesoscale front and local winds due to differential fluxes over land, cold shelf water, and warm Gulf Stream and also to examine how the meso-scale front feeds back to the ocean and modifies upper ocean temperature and current fields. Strong ocean responses induced by winter storms include significant changes in sea level, across-shelf and along-shelf currents, and turbulent mixing. Locally enhanced winds over a warm sea induce large surface heat fluxes which cool the upper ocean by up to 2 °C, mainly during the cold air outbreak period after the storm passage (Nelson et al. 2014). Detailed understanding of coastal circulation near Cape Hatteras under the influence of winter storms requires high-resolution space and time continuous realizations of ocean variables, from which quantitative dynamics can be gleaned. In this study, we take advantage of valuable in situ observations measured during the Frontal

Interactions Near Cape Hatteras (FINCH) program (Gawarkiewicz et al. 2009; Savidge and Austin 2007; Savidge et al. 2013a) and apply a regional ocean model to study Cape Hatteras coastal circulation response to different atmospheric forcing conditions in January 2005. Section 2 describes the ocean model configurations and model-observation comparisons. Detailed analyses on ocean transport and circulation dynamics are given in Sect. 3, followed by discussions in Sect. 4 and conclusions in Sect. 5.

2 Ocean model hindcast

2.1 Model configurations

A regional ocean circulation model was implemented for the MAB and SAB (hereafter MABSAB), covering the area between 81.89° W to 69.80° W and 28.41° N to 41.84° N (Fig. 1). The model is based on the Regional Ocean Modeling System (ROMS) (Shchepetkin and McWilliams 2005), a free-surface, terrain-following, primitive-equation ocean model in widespread use for estuarine, coastal and basin-scale

applications. The horizontal resolution of this model was 2 km. Model bathymetry was interpolated from National Geophysical Data Center (NGDC) 2-Minute Gridded Global Relief Data. Vertically, 36 terrain-following layers were used. Momentum advection equations were solved using a third-order upstream bias scheme for three-dimensional velocity and a fourth-order centered scheme for two-dimensional transport, whereas tracer (temperature and salinity) advections were solved with a third-order upstream scheme in the horizontal direction and a fourth-order centered scheme in the vertical direction. The horizontal mixing for both the momentum and tracer utilized the harmonic formulation with 100 and 20 m^2/s as the momentum and tracer mixing coefficient, respectively. Turbulent mixing for both momentum and tracers was computed using the Mellor/Yamada Level-2.5 closure scheme (Mellor and Yamada 1982). For open boundary conditions, the model was nested inside the 1/12 degree global data assimilative HYCOM/NCODA (Chassignet et al. 2007) output superimposed with the M_2 tide forcing derived from an ADCIRC tidal model (Luettich et al. 1991) simulation of the western Atlantic. M_2 tide is the dominant tidal constituent in this region (Lentz et al. 2001; Savidge et al. 2007), largely determining regional tidal mixing and rectification. Sponge layers were defined over 20 grid points from the eastern and southern boundaries, where the horizontal viscosity was increased linearly from values used in the model interior to a ten-fold increase at the boundaries. Within the sponge layer, three-dimesional tracer and momentum fields were nudged (Marchesiello et al. 2003) to corresponding HYCOM model fields.

With this regional model setup, we performed a MABSAB circulation hindcast for January 1, 2004 to February 28, 2005. This overlapped the time period of the FINCH observations (January 15 to February 2, 2005). The model's initial conditions were interpolated from HYCOM fields on January 1, 2004. One caveat we identified during the course of MABSAB ROMS implementation was a coastal salinity bias in HYCOM solution. When compared with the $0.25° × 0.25°$ HydroBase Hydrographic climatology (Curry 1996), HYCOM/NCODA was found to overestimate the coastal salinity field due to the lack of fresh river water input. For instance, HYCOM surface mean (averaged between 2004/1/1 and 2007/12/31) salinity was up to 2 (6) psu higher on the shelf (at major river mouths) than the corresponding HydroBase salinity values. Surface temperature differences between the HYCOM and HydroBase were seen as well, but to a smaller extent. Together, biases in salinity and temperature fields led to a bias in the density field, which in turn resulted in biases in the alongshore and cross-shelf pressure gradients. To correct for such biases, we replaced the HYCOM three-dimensional annual mean salinity and temperature fields with the corresponding HydroBase annual means. The sea surface height slope was accordingly revised using the geostrophic relationship, resulting in an enhanced along-shelf velocity at the eastern boundary north of 40° N. The model therefore produced a mean equatorward alongshelf flow, which was consistent with the earlier studies about the magnitude of the mean southward depth-averaged alongshelf flow on the MAB (e.g., Lentz 2008).

We focused on model hindcast results near Cape Hatteras in January 2005 to understand coastal circulation responses to two drastically different atmospheric forcing conditions. In situ observations from NDBC buoy 44014 (Fig. 2) showed that the wind was weak and generally northward (upwelling favorable) between January 1 and January 14. The mean east-west and north-south wind components during these 2 weeks were ~0.1 and 1.8 m/s, respectively. Both air and sea surface temperatures were relatively constant, around 11 °C. In contrast, from January 15 to January 31, there were four consecutive winter storms (downwelling favorable) passing through the area with wind speeds up to 15 m/s, which was representative of windiness at Cape Hatteras (Savidge et al. 2013b). The mean east-west and north-south wind components during these 2 weeks were 1.7 and −6.6 m/s, respectively. Compared to the first half of month, air temperature decreased by as much as 20 °C, whereas sea surface temperature decreased by up to 5 °C. In the following discussions, we refer the time between January 1 and January 14 as period I, and the time between January 15 and January 31 as period II to contrast coastal ocean responses.

Comparisons of model-simulated ocean surface temperature, salinity, sea surface height, and surface velocity fields between January 7 (representing period I) and January 22 (representing period II) show very different ocean states (Fig. 3). Significant shelf-wide water temperature decreases were seen in period II, especially in the southern MAB region. As a result of storm wind forcing which favored downwelling, low salinity coastal waters were pushed both southward and shoreward. Concurrently, coastal sea levels rose in both the MAB and SAB, which corresponded to strong surface velocity variations. On January 7, we saw significant cross-shelf flows, whereas on January 22, surface flows on both the MAB and SAB were moving southward. Strong storm forcing in period II also affected the Gulf Stream, by significantly reducing its surface velocity.

2.2 Model-data comparisons

To better evaluate model hindcast skills in January 2005, we compared model solutions against observations from the following sources: National Ocean Service (NOS) sea level data, which provided hourly measurement of water levels; and FINCH survey data from January 2005, including high-resolution temperature, salinity, and moored acoustic Doppler current profiler (ADCP) velocity observations.

Fig. 2 Time series of surface
wind, surface air temperature, and
sea surface temperature measured
by NDBC buoy 44014 in January
2005
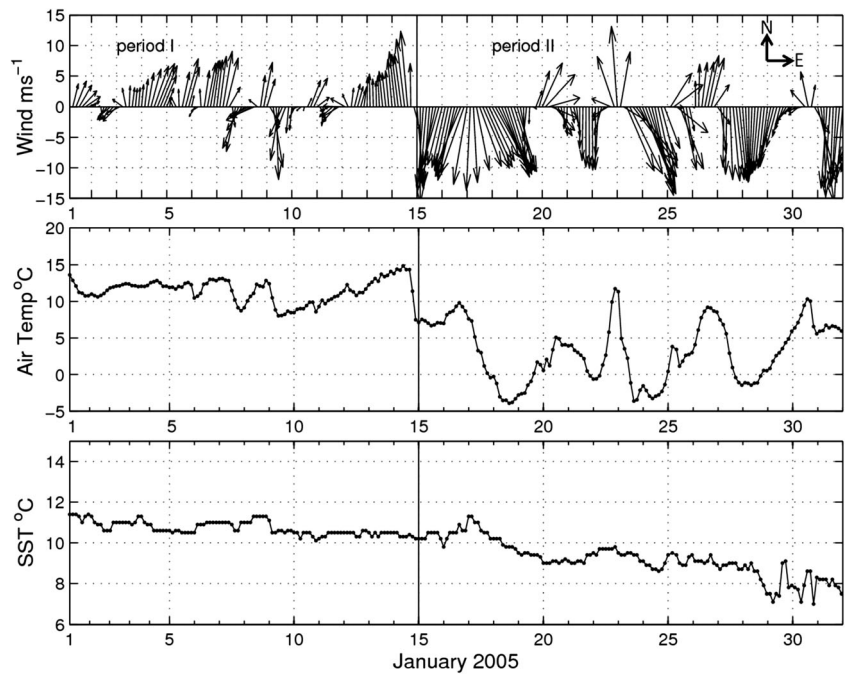
A number of statistical measures were used to quantitatively assess the model performance, including the correlation coefficient (R), the root mean square root error (RMSE), and the skill score. In particular, we defined the skill score following the method in Hetland and Dimarco (2012): $skill = 1 - \frac{\sigma_m^2}{\sigma_c^2}$,

where σ_m^2 is the model error variances and σ_c^2 is the climatology error variance. For a perfect model that reproduces the observation exactly, the model skill is 1, and if the model error is statistically similar to the deviation of the observations from climatology, the skill is 0.
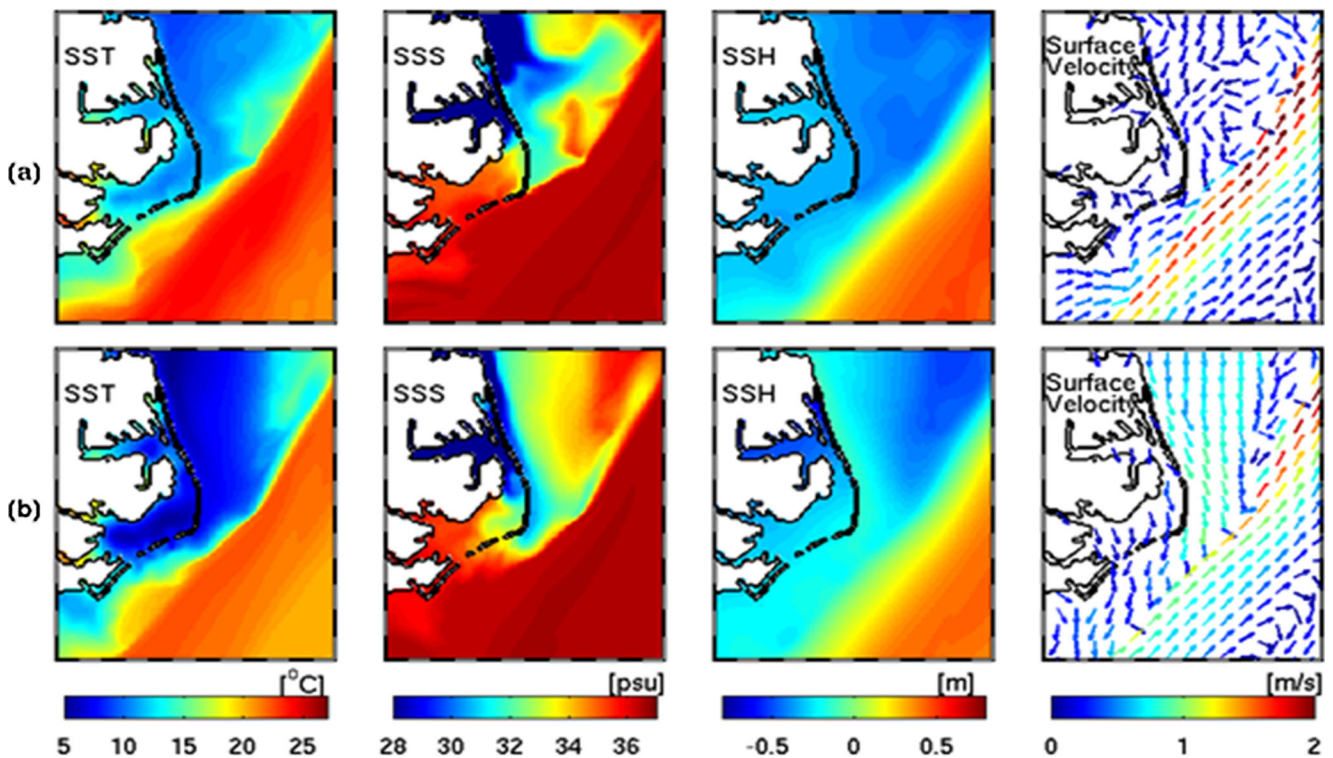
Fig. 3 Snapshots of simulated sea surface temperature (SST), sea surface salinity (SSS), sea surface height (SSH), and surface velocity on January 7 (**a**) and January 22 (**b**) 2005

Point-by-point comparisons of coastal sea level were made at several stations in the domain for hourly time series as well as 36-h low-pass filtered renditions (Fig. 4) to examine wind-driven Ekman and shelf wave dynamics (Gill 1982; Brink 1998). Such a validation shows that the model was able to resolve hourly sea level variations reasonably well. At the 95 % confidence interval, the correlation coefficients between the two hourly time series (unfiltered and filtered) were both above 0.86 at all these stations, and the model skill scores were between 0.7 and 0.8. The model also reproduced the spatial distribution of tidal phase and amplitude well, and the results were consistent with previous study on the tide near Cape Hatteras (Pietrafesa et al. 1985; Savidge et al. 2007). Reasonable comparisons were also found in the subtidal sea level comparisons. Except for Beaufort, NC, correlation coefficients were all larger than 0.6, and model skills were larger than 0.45. Beaufort station is in a complex bayou behind the Outer Bank and Atlantic Beach, and we speculate that the less accurate subtidal sea level comparison is due to complex coastal geometry, which cannot be accurately resolved by the current resolution of the model.

A towed undulating vehicle system (ScanFish) was used in the January 2005 survey by the FINCH program (details of data processing appeared in Gawarkiewicz et al. 2009). This instrument provided high-resolution water column temperature and salinity measurements along the ship's track. To compare with ScanFish T/S data collected on January 20, 25, and 29 (Fig. 5), we interpolated model-simulated temperature and salinity fields at the same sampling locations used by the FINCH survey. Because the model output was archived every 12.42 h (M_2 tidal period), whereas the ScanFish T/S data were instantaneous measurements, we expected some temporal aliasing issues in this comparison. Nevertheless, comparisons show that the model was capable of capturing major spatial features in the along- and across-shelf temperature and salinity distributions, such as the warm, salty Gulf Stream water seaward of the shelfbreak, and cold, fresher MAB water on the shelf. The model underpredicted the stratification over Diamond Shoals on January 20, where there was warm, salty bottom water between 100- and 1,000-m isobaths, likely a result of Gulf Stream intrusion (Gawarkiewicz et al. 1992; Lentz 2003). Subsequent T/S comparisons on January 25 and 29 are better than those on January 20. The temperature RMSE was around 1 °C, and salinity RMSE was around 0.7 psu. One model deficiency we note was that the simulated salinity at the offshore tip of the southernmost cross-shelf transect was 1–2 psu fresher than observed, suggesting that the model had more freshwater export into the Gulf Stream at this location than was actually the case.

The FINCH program also collected velocity observations from two acoustic Doppler current meter moorings (mooring 5004 and 5042; see Fig. 1) at 30-m depth in the last week of January. A 36-h truncated FFT low-pass filter was applied to both observed and simulated east-west and north-south velocity components at these two locations. Because the local isobaths change orientation moving from MAB to SAB, strong along-shelf flows were seen in the north-south velocity component at mooring 5004 and in the east-west velocity component at mooring 5024 on January 24 and 28–29 in response to storm forcing. Comparisons (Fig. 6) show that such temporal variations were resolved by the model. Quantatively, we calculated that the correlation coefficient was around 0.7, and the model skill varied from 0.25 to 0.6. Finally, FINCH observations showed that the core of MAB shelfbreak jet had a velocity of −0.51 m/s (moving equatorward) and its relative vorticity was of o(1) normalized by the Coriolis parameter (Gawarkiewicz et al. 2009). The model resolved the MAB shelfbreak jet quite realistically, with a

Fig. 4 Comparisons of observed (blue) and simulated (red) sea levels at four stations near Cape Hatteras. The left column shows the hourly time series comparison, while the right column shows comparisons of 36-h low-pass filter renditions. R values representing the correlation coefficient (95 % confidence interval) between observation and simulation are given in each panel
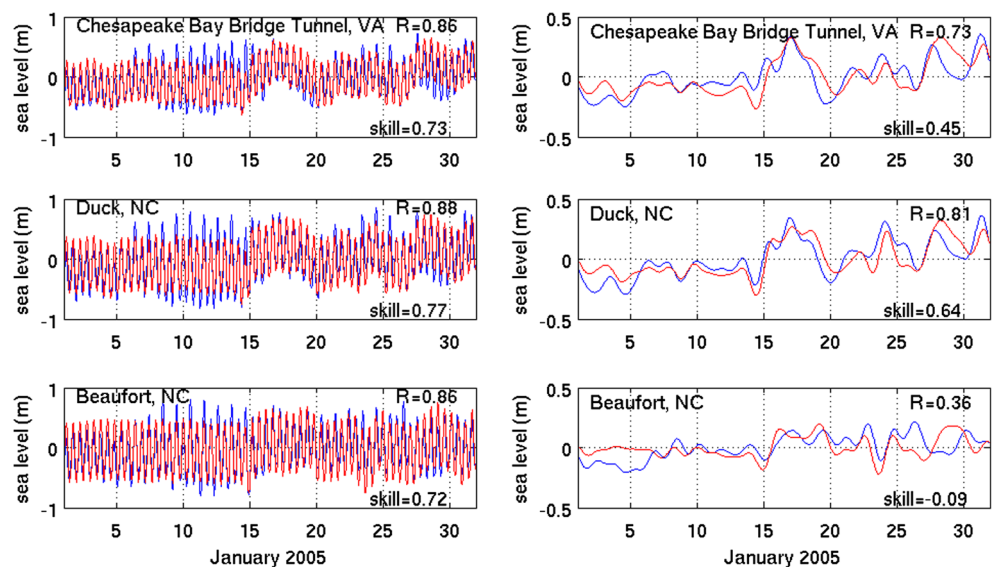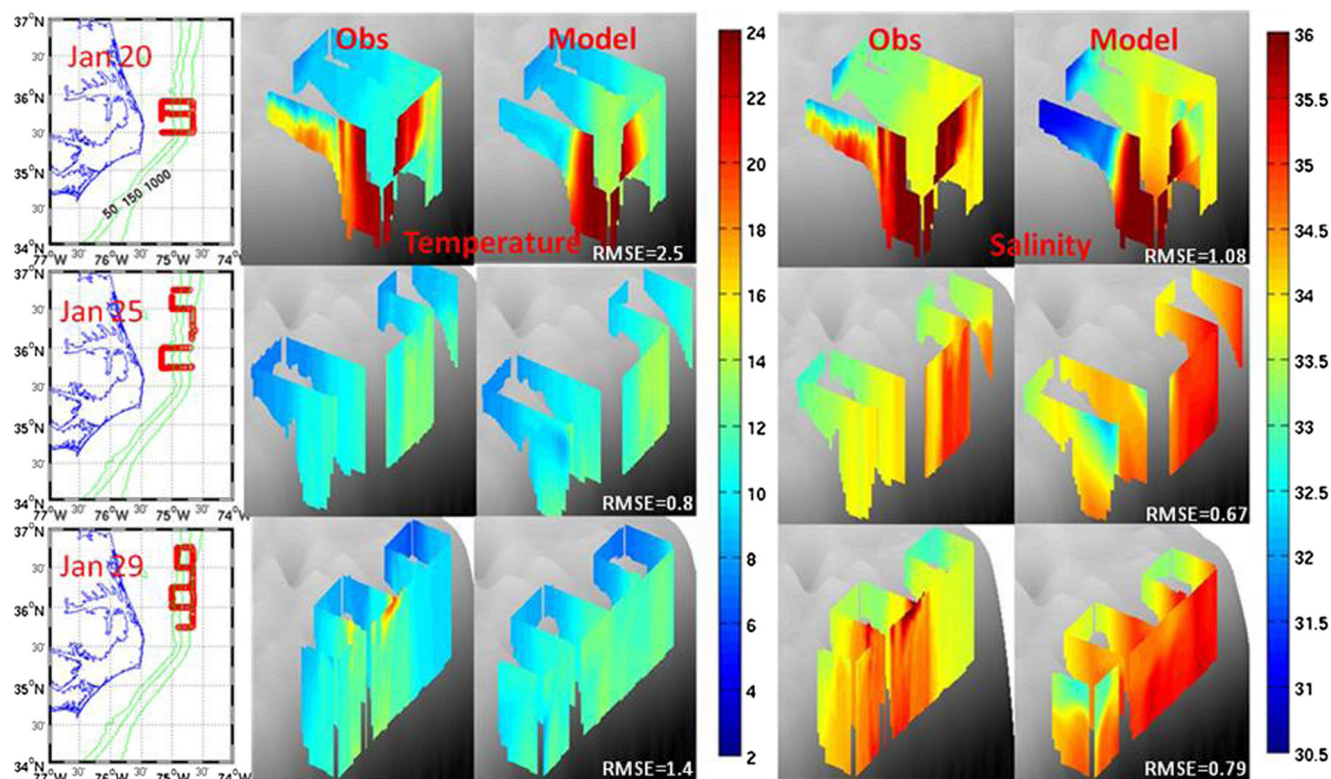
Fig. 5 Three-dimensional temperature and salinity comparisons between the model hindcast and FINCH ScanFish survey data on January 20th (*top panels*), 25th (*middle panels*), and 29th (*lower panels*). Locations of observations (ship tracks) are shown in the *left column*. The RMSE unit of temperature is °C and salinity is psu

maximum velocity around −0.50 m/s, and had a same order of relative vorticity as the observation (not shown).

Due to the presence of different water masses, ocean fronts, and the boundary current, hydrographic conditions and circulation dynamics in our study domain are very complex and challenging to simulate. Our model had done a reasonably good job in reproducing observed features both qualitatively and quantitatively. This led confidence for the circulation dynamics analyses discussed in the following sections. We investigated the along- and across-shelf transports, momentum balance, and kinetic energy budgets to characterize ocean responses to drastically different atmospheric forcing between the first and second half of January 2005.

3 Circulation dynamic analyses

3.1 Transport analysis

To compute the along-shelf transport in January 2005, we selected three across-shelf transects in the vicinity of Cape Hatteras (Fig. 1 inset). Transects 1–3 were perpendicular to cross-shelf lines at Virginia Beach (36.9° N), Cape Hatteras (35.4° N), and Cape Lookout (34.6° N), respectively. All three transects were between the coastline and the 100-m isobath

(which was considered the boundary between the shelf and slope). The cross-shelf distances of three transects were 112.2 km (transect 1), 27.3 km (transect 2), and 58.0 km (transect 3), respectively, and the corresponding subsurface areas of these transects are 3.16×10^6 m^2 (transect 1), 0.90×10^6 m^2 (transect 2), and 1.93×10^6 m^2 (transect 3), respectively.

Earlier study by Kim et al. (2001) based on velocity observations during the Ocean Margins Program (Bauer 2002) estimated the mean southward along-shelf transport from February to May 1996 at a nearby 36.7° N transect to be 0.17 Sv. Our simulated along-shelf transport values (based on 36-h low-pass filtered velocity) at the three transects were much larger (Fig. 7), producing monthly mean transports of −0.42 Sv (alongshore to the southward), 0.35 Sv (alongshore to the northward), and 0.41 Sv (alongshore to the northward) at three transects, respectively. We note that significant increases in southward (or decreases in northward) transport occured at all three transects in period II, in response to strong downwelling favorable storm wind forcing. In period I, the mean alongshelf transports at the three transects were −0.01, 0.59, and 0.57 Sv, as opposed to −0.79, 0.14, and 0.26 Sv in period II. The large southward transport in period II from transect 1 compared favorably with the total shelf transport estimated from FINCH observations, Gawarkiewicz et al. (2009) reported 0.61 Sv over the shelf and 0.27 Sv in the shelfbreak jet for a total southward transport of 0.88 Sv.
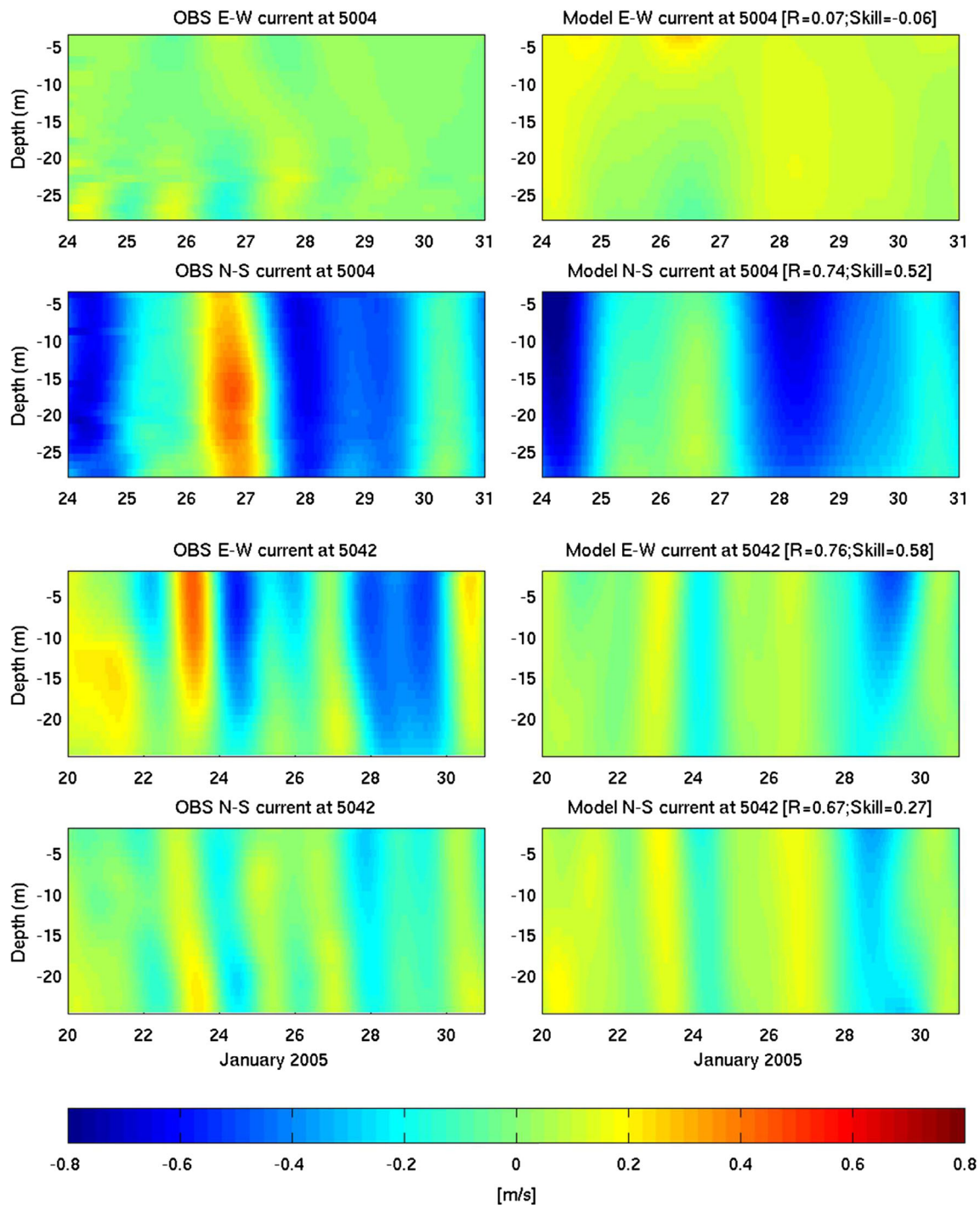
Fig. 6 Time series comparisons of simulated and observed north-south and east-west velocity components. Observations were taken by FINCH ADCP moorings (5004 and 5042) in the last week of January 2005. *R* values representing the correlation coefficient (95 % confidence interval) between observation and simulation are given in each panel

Because of flow continuity, variations in along-shelf transport induced corresponding cross-shelf transport changes. Using the 100-m isobath as the shelf-slope boundary, we defined the line connecting the two offshore end points of cross-shelf transects 1 and 2 as the along-shelf transect N, and similarly the section connecting the offshore end points of cross-shelf transects 2 and 3 as along-shelf transect S (Fig. 1). Time series of computed cross-shelf transport were quite different between transects N and S (Fig. 7) in January 2005, with monthly mean cross-shelf transport values at transects N and S being 0.77 and 0.05 Sv, respectively. This suggests that transect N was the major shelf water export site during the

Fig. 7 Time series of simulated along-shelf transport (Sv) at transects 1–3 (*upper panel*) and cross-shelf transport at transects N and S in January 2005. Positive values represent the alongshore northward (or across-shelf eastward) flow and negative values represent the alongshore southward (or across-shelf westward) flow
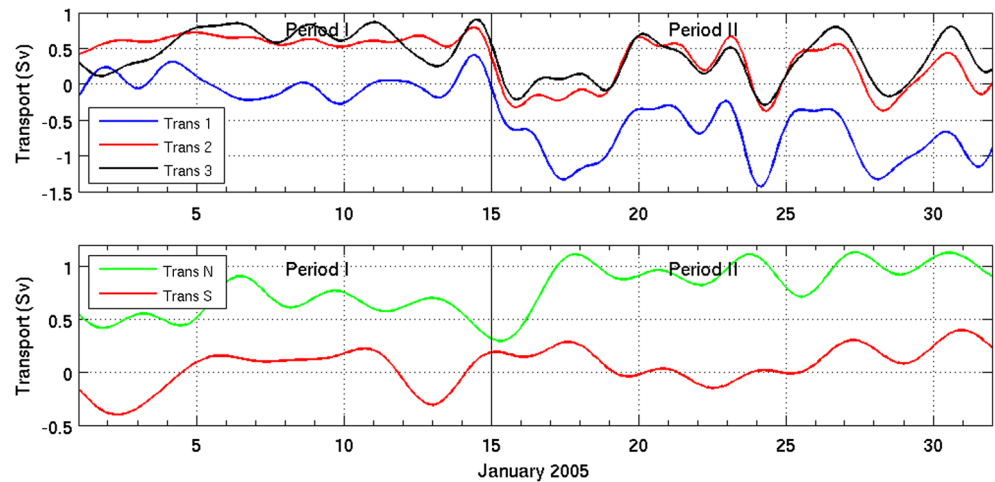
study period. The flow convergence caused by the northward flow across transect 2 in period I and the southward flow across transect 1 in period II was well-correlated with the offshore transport across transect N, consistent with earlier seasonal convergence calculations (Savidge and Bane 2001; Savidge and Savidge 2014).

We can decompose the along-shelf velocity into geostrophic and ageostrophic components. At transect 1 (Fig. 8), the along-shelf geostrophic velocity component can be computed as $v_g = -\frac{1}{f\rho}\frac{\partial p}{\partial x}$ from the model, and the ageostrophic velocity component is the difference between the total along-shelf velocity and geostrophic velocity. As expected, the along-shelf velocity was dominated by its geostrophic component in both periods. The geostrophic velocity in period I had an interesting layered structure on the inner shelf (~75.8° W) due to the presence of a freshwater plume, with a baroclinic structure in which the surface flow moved southward while the bottom flow moved northward. This was different on the mid-shelf and outer-shelf, where water over the entire column flowed southward or northward. The northward flow on the outer-shelf was presumably related to the influence of Gulf Stream meanders. There, the ageostrophic component was much weaker than its geostrophic counterpart. The ageostrophic component was primarily located in the surface and bottom boundary layers and was generated by surface and
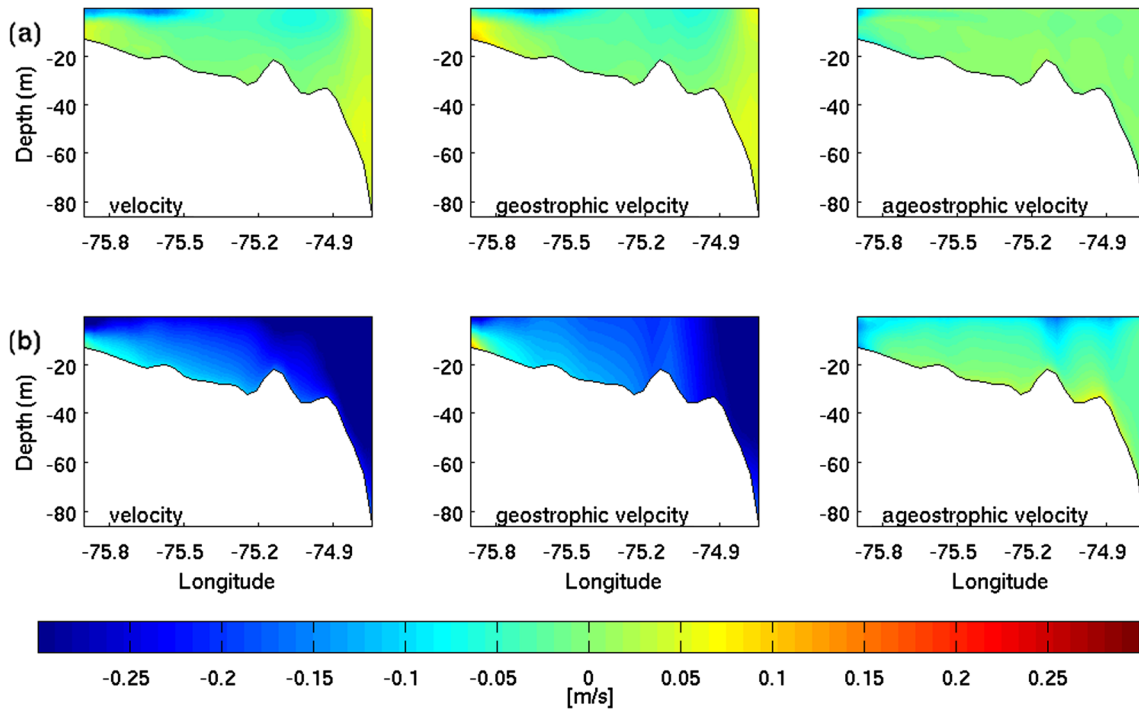
bottom stresses by virtue of Ekman balance. In period II, when strong southward, downwelling-favorable winds significantly built up coastal sea level, the corresponding geostrophic currents became much stronger and flowed uniformly southward over almost the entire shelf. The ageostrophic component drastically increased too. The bottom ageostrophic currents flowed northward, counteracting the southward-flowing geostrophic velocity. The contributions of geostrophic and ageostrophic components will be further studied in Sect. 3.2 below.

3.2 Momentum analysis

Based on in situ observations, Lentz et al. (1999) divided the shallow portion of the North Carolina shelf into three dynamically distinct regions based on momentum budget differences: the surf zone, the inner shelf (between the surf zone and the 13-m isobath), and the mid-shelf. It is found that for the mid-shelf, the along-shelf momentum balance was dominated by along-shelf wind stress, the pressure gradient, and bottom stress. The cross-shelf momentum balance was predominantly geostrophic, which was also validated in the SAB shelf (Lee et al. 1989). Here, we performed a similar momentum analysis based on model hindcast solutions. Vertically integrating the horizontal momentum equation gives

$$
\int_{-h}^{\zeta}\frac{\partial u}{\partial t}\,dz + \int_{-h}^{\zeta}u\frac{\partial u}{\partial x}\,dz + \int_{-h}^{\zeta}v\frac{\partial u}{\partial y}\,dz + \int_{-h}^{\zeta}w\frac{\partial u}{\partial z}\,dz - \int_{-h}^{\zeta}fv\,dz = \int_{-h}^{\zeta}\left(-\frac{1}{\rho_0}\frac{\partial p}{\partial x}\right)dz + \int_{-h}^{\zeta}\frac{\partial}{\partial z}\left(K_m\frac{\partial u}{\partial z}\right)dz + \int_{-h}^{\zeta}D_u\,dz
$$

$$
\int_{-h}^{\zeta}\frac{\partial v}{\partial t}\,dz + \int_{-h}^{\zeta}u\frac{\partial v}{\partial x}\,dz + \int_{-h}^{\zeta}v\frac{\partial v}{\partial y}\,dz + \int_{-h}^{\zeta}w\frac{\partial v}{\partial z}\,dz + \int_{-h}^{\zeta}fu\,dz = \int_{-h}^{\zeta}\left(-\frac{1}{\rho_0}\frac{\partial p}{\partial y}\right)dz + \int_{-h}^{\zeta}\frac{\partial}{\partial z}\left(K_m\frac{\partial v}{\partial z}\right)dz + \int_{-h}^{\zeta}D_v\,dz
$$

$$(1)$$

Fig. 8 Sectional views of time-averaged along-shelf velocity, along-shelf geostrophic velocity, and along-shelf ageostrophic velocity at transect 1 in period I (**a**) and period II (**b**)

where D_u and D_v are the horizontal mixing, K_m is the vertical eddy viscosity coefficient, $h(x,y)$ is the bottom depth, and $\zeta(x,y,t)$ is the surface elevation.

If we define the depth-averaged velocity as

$$\overline{u} = \frac{1}{h+\zeta} \int_{-h}^{\zeta} u \, dz$$

$$\overline{v} = \frac{1}{h+\zeta} \int_{-h}^{\zeta} v \, dz$$

vertically integrated nonlinear advection as

$$A_x = \int_{-h}^{\zeta} \left(u\frac{\partial u}{\partial x} + v\frac{\partial u}{\partial y} + w\frac{\partial u}{\partial z} \right) dz$$

$$A_y = \int_{-h}^{\zeta} \left(u\frac{\partial v}{\partial x} + v\frac{\partial v}{\partial y} + w\frac{\partial v}{\partial z} \right) dz$$

vertically integrated pressure gradient as

$$P_x = \int_{-h}^{\zeta} \left(-\frac{1}{\rho_0}\frac{\partial p}{\partial x} \right) dz$$

$$P_y = \int_{-h}^{\zeta} \left(-\frac{1}{\rho_0}\frac{\partial p}{\partial y} \right) dz$$

and vertically integrated horizontal mixing as

$$D_x = \int_{-h}^{\zeta} D_u \, dz$$

$$D_y = \int_{-h}^{\zeta} D_v \, dz$$

and apply both the surface and bottom conditions, we can rewrite the depth-averaged momentum equations as

$$\frac{\partial \overline{u}}{\partial t} + \frac{A_x}{h+\zeta} - f\overline{v} = \frac{P_x}{h+\zeta} + \frac{\tau^{sx}}{\rho_0(h+\zeta)} - \frac{\tau^{bx}}{\rho_0(h+\zeta)} + \frac{D_x}{h+\zeta}$$

$$\frac{\partial \overline{v}}{\partial t} + \frac{A_y}{h+\zeta} + f\overline{u} = \frac{P_y}{h+\zeta} + \frac{\tau^{sy}}{\rho_0(h+\zeta)} - \frac{\tau^{by}}{\rho_0(h+\zeta)} + \frac{D_y}{h+\zeta}$$

$$(2)$$

The left side of the above Eq. (2) includes the acceleration term, nonlinear advection, and Coriolis force term, and the right side of the equations includes the pressure gradient term, the wind stress term, bottom stress term, and the horizontal mixing term. Each term in this diagnostics was calculated e at

the model's sigma level and subsequently depth-averaged before the analysis.

To highlight differences in momentum balances between the two periods, we time averaged each term over period I and period II (Fig. 9). For both u- (east-west veclocity component) and v- (north-south velocity component) momentum equations, the two largest terms were the Coriolis term and the pressure gradient term, and they generally balanced each other. The residual after calculating the sum of Coriolis and pressure gradient force terms constitutes the ageostrophic momentum, which was balanced by local acceleration, nonlinear advection, surface and bottom stress, and horizontal mixing. The depth-averaged momentum term was larger on the shelf than in the deep ocean. The temporal mean acceleration terms in period I and period II were small. The nonlinear advection terms were relatively noisy, containing many small-scale variations. Their largest values were seen in
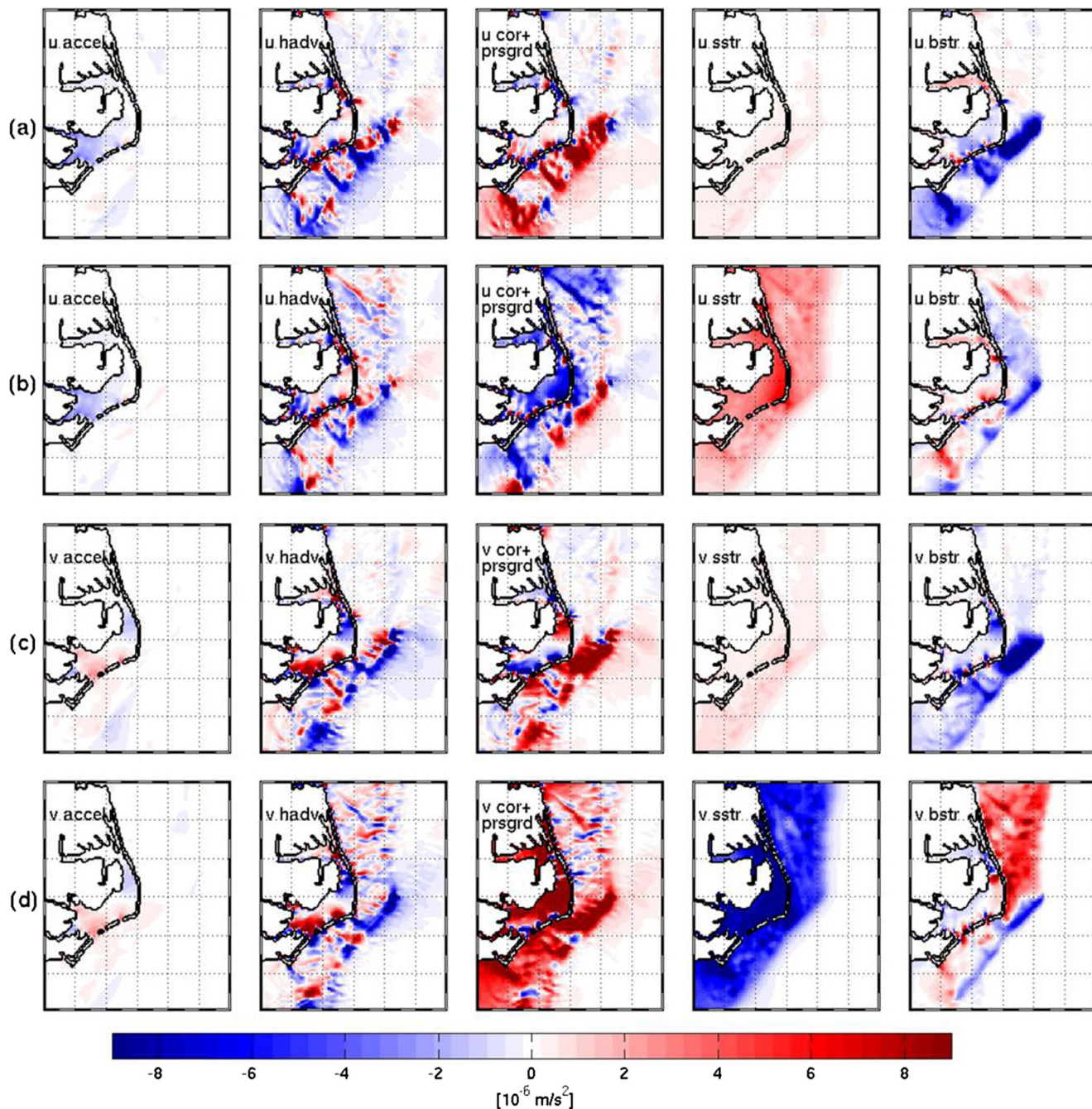
Fig. 9 Spatial views of temporal mean depth-averaged u-momentum balance in period I (a) and period II (b) and v-momentum balance in period I (c) and period II (d). Shown from *left to right* are the acceleration term (accel), nonlinear advection term (hadv), summation of Coriolis and pressure gradient term (cor+prsgrd), wind stress term (sstr), and bottom stress term (bstr)

the SAB along the Gulf Stream and at the entrances of shallower estuaries. The effects of wind stress and bottom stress were most clearly present on the shelf. Note that the shelf-wide surface wind stress in period II increased up to 5 times of that in period I. Because of the quadratic law used by the model, the bottom stress was proportional to the square of bottom velocity. The largest bottom stress was seen to be associated with the Gulf Stream in the SAB. In period II, strong storms led to much larger bottom velocity in the alongshelf direction (Fig. 9d), and subsequently significantly enhanced bottom stress. The shelf-wide ageostrophic balance during period I was achieved between nonlinear advection and bottom stress, whereas the balance during period II was accomplished jointly by nonlinear advection and surface and bottom stresses.

3.3 Energy analysis

Energy conservation is one of the most fundamental laws of nature. Energy in the ocean can be classified into two major parts: mechanical and internal energy. Mechanical energy consists of two parts: kinetic energy (KE) and gravitational energy. On the global scale, wind stress and tidal forcing are the two most important sources of mechanical energy that drive ocean circulation. Although the mechanical energy flux is 1,000 times smaller than heat flux, it controls the strength of ocean circulation (Huang 2004). MacCready et al. (2009) showed that mechanical energy budget analysis provides an insightful means to explore tidal- and wind-induced mixing in estuaries and shelf areas. We applied the same method to characterize the nature of Cape Hatteras shelf circulation in periods I and II of January 2005.

Following MacCready et al. (2009), we omitted the horizontal mixing term (which was negligibly small). Multiplying u and v to the corresponding momentum equation, we have

$$u\frac{du}{dt} - fvu = -\frac{u}{\rho_0}\frac{\partial p}{\partial x} + u\frac{\partial}{\partial z}\left(K_m\frac{\partial u}{\partial z}\right)$$
$$v\frac{dv}{dt} + fuv = -\frac{v}{\rho_0}\frac{\partial p}{\partial y} + v\frac{\partial}{\partial z}\left(K_m\frac{\partial v}{\partial z}\right) \quad (3)$$

The two equations of Eq. (3) can be combined as

$$\frac{d}{dt}\left(\frac{1}{2}\rho_0 u^2 + \frac{1}{2}\rho_0 v^2\right) = \left(-u\frac{\partial p}{\partial x} - v\frac{\partial p}{\partial y}\right) + \rho_0 u\frac{\partial}{\partial z}\left(K_m\frac{\partial u}{\partial z}\right) \quad (4)$$
$$+ \rho_0 v\frac{\partial}{\partial z}\left(K_m\frac{\partial v}{\partial z}\right)$$

Next, volume integrating this equation gives

$$\int_V \frac{dKE}{dt}dV = \int_V\left(-u\frac{\partial p}{\partial x} - v\frac{\partial p}{\partial y}\right)dV \quad (5)$$
$$+ \int_V\left(\rho_0 u\frac{\partial}{\partial z}\left(K_m\frac{\partial u}{\partial z}\right) + \rho_0 v\frac{\partial}{\partial z}\left(K_m\frac{\partial v}{\partial z}\right)\right)dV$$

where the KE is defined as

$$KE = \left(\frac{1}{2}\rho_0 u^2 + \frac{1}{2}\rho_0 v^2\right) \quad (6)$$

Following the method of MacCready et al. (2009), the term on the left side of the Eq. (5) can be derived as the KE storage and KE advection terms, and the second and third terms on the right side of the equation can be derived as wind stress work and dissipation terms. That is

$$\int_V \frac{dKE}{dt}dV = \frac{\partial}{\partial t}\left(KE_v dV\right) + \int_{A_{open}}\left(KE_v\right)u_n dA \quad (7)$$

$$\int_V\left(\rho_0 u\frac{\partial}{\partial z}\left(K_m\frac{\partial u}{\partial z}\right) + \rho_0 v\frac{\partial}{\partial z}\left(K_m\frac{\partial v}{\partial z}\right)\right)dV$$
$$= \int_{A_0}\left(u\tau^x + v\tau^y\right)\big|_{z=\eta}dA - \int_V\rho_0 K_m\left(u_z^2 + v_z^2\right)dV \quad (8)$$

Then, the vertically integrated mechanical energy equation can be rewritten as

$$\frac{\partial}{\partial t}\left(KE_v dV\right) = -\int_{A_{open}}\left(KE_v\right)u_n\, dA + \int_V\left(-u\frac{\partial p}{\partial x} - v\frac{\partial p}{\partial y}\right)dV$$
$$+ \int_{A_0}\left(u\tau^x + v\tau^y\right)\big|_{z=\eta}\, dA - \int_V\rho_0 K_m\left(u_z^2 + v_z^2\right)dV$$
$$(9)$$

representing the balance between KE storage (or the time rate of the KE change) on the left side, and the sum of the advection of the KE (first term on the right side), horizontal pressure work (PW, second term on the right side), wind stress work (third term on the right side), and dissipation due to the bottom friction and vertical mixing (fourth term on the right side). To check our caculations, we added all the terms in this KE equation together. The residual was not exactly 0 due to numerical round off error but was indeed several orders of magnitude smaller than each of the KE budget terms.

Each of the KE budget terms were calculated from the model output history and diagnostic files. Figure 10 shows the spatial distributions of time- and depth- averaged KE budget terms for period I (Fig. 10a) and period II (Fig. 10b). In period I, the time rate of KE change was in general positive, and in period II, the time rate of KE change was in general negative. The largest values of advection work (ADV) and PW occurred in the Gulf Stream area, and they generally balanced each other. In
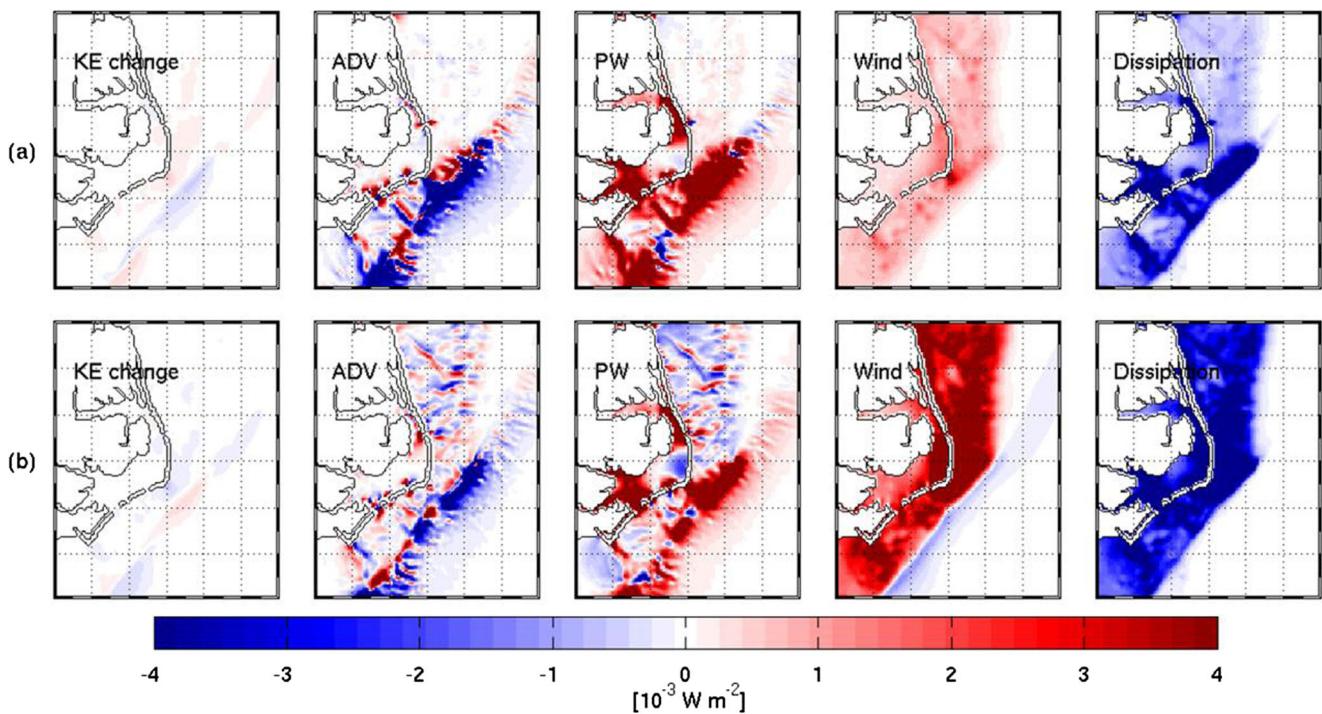
Fig. 10 Spatial view of the time- and depth-averaged kinetic energy budget terms in period I (**a**) and period II (**b**). Shown from *left to right* are the KE storage term (KE change), nonlinear advection work (ADV), pressure work (PW), wind stress work (Wind), and dissipation work (Dissipation)

both periods, the wind stress work was positive on the shelf, suggesting that the large-scale mean winds blew in the same direction as mean shelf current. Winds were much stronger in period II, resulting in much larger wind stress work on the shelf. By the opposite argument, because the mean wind flowed in the opposite direction of the Gulf Stream, the wind stress work was negative in the Gulf Stream area (Fig. 10b). The dissipation work was negative in both periods, and the largest values were seen

in the Gulf Stream area. Similar to the wind stress work, the dissipation work was larger on the shelf during period II than period I.

To understand how the shelf circulation KE budget varied over time, we now focus on the region shallower than 100 m. This part of the coastal ocean has an area of 5.3×10^{10} m^2 and a volume of 8.9×10^{11} m^3. Temporal variations of the MAB and SAB shelf area-averaged KE budget are shown in Fig. 11. High-frequency variations in

Fig. 11 Time series of the MAB (**a**) and SAB (**c**) shelf (shallower than 100 m) area averaged depth-integrated kinetic energy term budgets, and their corresponding subtidal term budgets on the MAB (**b**) and SAB (**d**) in January 2005. Term notations are the same as in Fig. 10. Also shown is the time series of the residual term, which was several orders of magnitude smaller than the other terms, indicating that the KE budget analysis was robust
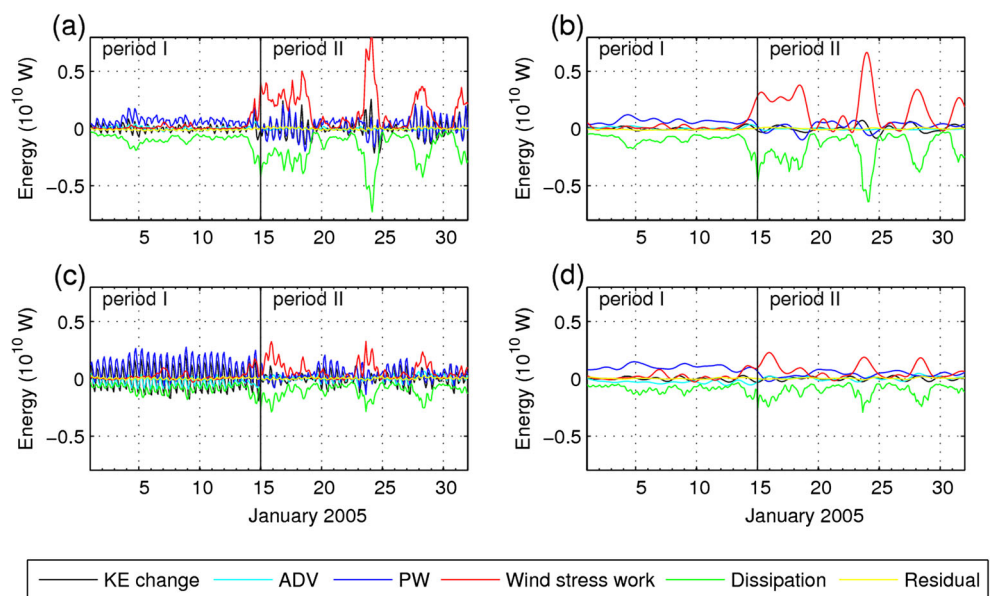
both the KE change term and PW were related to the M_2 tidal sea level change. In period I, the dominant terms were KE storage, PW, and dissipation work, whereas in period II, the wind work and dissipation work became the most dominant terms. As shown earlier, both wind stress work and dissipation work got amplified in period II, and as expected, they constituted the major energy balance during the stormy second half of January 2005. Throughout the month, the area-averaged ADV played a small role in the shelf KE budget. For the subtidal KE budget, the KE storage term became much smaller, and the dominant terms were PW and dissipation work in period I and wind stress and dissipation work in period II. The dominant KE balance terms were the same on the MAB shelf and on the SAB shelf, though the amplified magnitude of the wind stress work and dissipation work from period I to period II were smaller on SAB shelf than on MAB shelf. This is because the mean current on the SAB shelf is northward and is against the southward wind stress; therefore, wind stress work was offset on the SAB during the winter storm.

4 Discussions

Numerous model sensitivity experiments (using different atmosphere forcing products and open boundary conditions) were performed, indicating that hydrographic conditions, sea level, and coastal circulation near Cape Hatteras are sensitive to the exact locations of the Gulf Stream and its meanders. With regards to the Gulf Stream meander, Savidge (2004) showed that the energetic meanders of 3–8-day period, 180–380-km wavelength propagated downstream along the Gulf Stream at speeds of 40–55 km/day. The coastal sea level variations along the US mid-Atlantic coast were found to be influenced by variations in the Gulf Stream on timescales ranging from a few months to decades from observations (Andres et al. 2013; Ezer et al. 2013) and climate models (Yin et al. 2009). In this study, the location and magnitude of model simulated Gulf Stream agreed reasonably well with satellite altimetry observations (not shown) in the month of January 2005; no obvious Gulf Stream meander was identified, and the shelf circulation was largely determined by local forcing associated with winter storm passage. Examining the model's ability in simulating the Gulf Stream and its meanders over a longer timescale is an ongoing effort, and we will report our finding in a future correspondence.

Several features of the model solutions could be improved for greater accuracy. Compared with Hatteras Front observations (Savidge et al. 2013a), while the model was able to resolved the Hatteras Front with consistent front width and temperature and salinity gradients, the vertical mixing in the model appeared to be too strong, compromising the model's skill in resolving the detailed subsurface front structures (not

shown). Comparisons with the FINCH ScanFish hydrographic data showed that the model missed warm, salty bottom water over Diamond Shoals. This feature was likely related to Gulf Stream water subsurface intrusion. Future effort in improving model's skill will include assimilating sea surface height from satellite altimetry and other in situ observations (e.g., HF Radar, ship hydrographic observations) to better constrain model fields. The newly available four-dimensional variational (4DVAR) data assimilation technique has been successfully applied in MAB circulation studies (e.g., Zhang et al. 2010; Chen et al. 2014). Another way to improve the model is to refine the analysis of surface forcing by considering air-sea coupling during strong winter storms, such as those that occurred in period II. Nelson and He (2012) coupled ROMS data with the Weather Research and Forecast model. Air-sea coupled model simulations were performed for the same January 2005 period and showed that the ocean played an important role in shaping coastal wind and heat flux fields, which in turn affected the shelf water stratification and velocity fields. Additional information on ocean processes near Cape Hatteras would also help to refine model predictions. Ford (1952) first reported that MAB shelf water can be entrained by the Gulf Stream east of Cape Hatteras. Our model simulation clearly showed the presence of this kind of entrainment (Fig. 3). These entrained shelf waters mixed with the Gulf Steam, but details of their mixing processes and the fate of these shelf waters deserve further study. Other unanswered questions are how often and how much of the MAB shelf waters move into the SAB. Pietrafesa et al. (1994) suggested that the MAB waters "often" pass by Cape Hatters and enter the SAB. Our preliminary surface particle trajectory calculation (not shown) in January 2005 suggested that the MAB waters that entered the SAB were also entrained in the Gulf Stream, in a way similar to the surface circulation pattern suggested by Gray and Cerame-Vivas (1963). The three-dimensional ocean Lagrangian transport pathway near Cape Hatteras is therefore another important topic needing to be further explored.

Regardless of subtle solution differences in all the model sensitivity experiments we have done, comparisons of transport/momentum/energy budget analyses associated with each model experiment show that the patterns and trend in the dominated balances stay the same, suggesting that the underlying circulation dynamics we discussed in Sect. 3 is robust and meaningful.

5 Summary

We used a realistic regional ocean circulation model to hindcast the circulation near Cape Hatteras, North Carolina, in January 2005. Model results were compared with observed coastal sea level, temperature, salinity, and velocity data.

Reasonably good agreement was found, indicating that the model has intrinsic prediction skill for regional circulation. With time- and space-continuous model solutions, we performed analyses of along- and cross-shelf transport, momentum, and energy balance diagnoses to quantify coastal ocean responses to different atmospheric forcing conditions in January 2005. The model results show that the first half of month (period I, January 1–14) was characterized by light, upwelling favorable wind, whereas the second half (period II, January 15–31) was characterized by consecutive storms with strong southward, downwelling favorable winds. In terms of shelf water transport, during the stormy period II, both southward along-shelf transport and cross-shelf transport significantly increased. The along-shelf transport change was mainly due to the geostrophic velocity change associated with the coastal sea level setup. In terms of momentum balance, wind stress was mainly balanced by bottom friction and the residual of the Coriolis and pressure gradient forces. During period I, the dominant KE balance on the shelf was between the time rate of KE change and PW, whereas during the stormy period II, the main shelf KE balance was achieved between wind stress work and dissipation work.

References

Andres M, Gawarkiewicz GG, Toole JM (2013) Interannual sea level variability in the western North Atlantic: regional forcing and remote response. Geophys Res Lett 40:5915–5919. doi:10.1002/2013GL058013

Bauer JE (2002) Biogeochemistry and cycling of carbon in the northwest Atlantic continental margin: findings of the Ocean Margins Program. Deep-Sea Res II 49:4271–4709

Brink KH (1998) Wind-driven currents over the continental shelf. In: Brink KH, Robinson AR (eds) The Sea, 10, 3–20. Wiley, N.Y

Chao S-Y (1992) An air-sea interaction model for cold air outbreaks. J Phys Oceanogr 22:821–841

Chassignet EP, Hurlburt HE, Martin Smedstad O, Halliwell GR, Hogan PJ, Wallcraft AJ, Baraille R, Bleck R (2007) The HYCOM (HYbrid Coordinate Ocean Model) data assimilative system. J Mar Syst 65: 60–83

Chen K, He R, Powell B, Gawarkiewicz G, Moore AM, Arango HG (2014) Data assimilative modeling investigation on Gulf Stream Warm Core Ring interaction with continental shelf and slope circulation. J Geophys Res: Oceans. doi:10.1002/ 2014JC009898

Churchill JH, Berger TJ (1998) Transport of Middle Atlantic Bight shelf water to the Gulf Stream near Cape Hatteras. J Geophys Res 103(C13):30,605–30,621. doi:10.1029/98JC01628

Curry RG (1996) HydroBase: a database of hydrographic stations and tools for climatological analysis. Technical Report WHOI-96-01, Woods Hole Oceanographic Institution, 44 pp

Dirks RA, Kuettner JP, Moore JA (1988) Genesis of Atlantic Lows Experiment (GALE): an experiment. Bull Am Meteorol Soc 69:148–160

Ezer T, Atkinson LP, Corlett WB, Blanco JL (2013) Gulf Stream's induced sea level rise and variability along the US mid-Atlantic coast. J Geophys Res 118(2):685–697. doi:10.1002/jgrc.20091

Fisher A Jr (1972) Entrainment of shelf water by the Gulf Stream Northeast of Cape Hatteras. J Geophys Res 77(18):3248–3255. doi:10.1029/JC077i018p03248

Ford WL (1952) On the nature, occurrence and origin of cold low salinity water along the edge of the Gulf Stream. J Mar Res 11:281–293

Gawarkiewicz G, Church TM, Luther GW, Ferdelman TG, Caruso M (1992) Large-scale penetration of Gulf Stream water onto the Continental Shelf north of Cape Hatteras. Geophys Res Lett 19(4): 373–376

Gawarkiewicz GG, Churchill JH, Bahr FB, Linder CA, Marquette CD (2009) Shelfbreak frontal structure and processes north of Cape Hatteras in winter. J Mar Res 66:755–799

Gill AE (1982) Atmosphere Ocean Dynamics. Academic Press, 662 pp

Gray IE, Cerame-Vivas MJ (1963) The circulation of surface waters in Raleigh Bay, North Carolina. Limnol Oceanogr 8:330–337

Hetland RD, DiMarco SF (2012) Skill assessment of a hydrodynamic model of circulation over the Texas- Louisiana continental shelf. Ocean Model 43–44:64–76. doi:10.1016/j.ocemod.2011.11.009

Huang RX (2004) Ocean, energy flows in. Encyclopedia of Energy, C. J. Cleveland, Ed., Vol. 4, Elsevier, 497–509

Kim YY, Weatherly GL, Pietrafesa LJ (2001) On the mass and salt budgets for a region of the continental shelf in the southern Mid-Atlantic Bight. J Geophys Res 106:31,263–31,282. doi:10.1029/2000JC000738

Kupferman SL, Garfield N (1977) Transport of low-salinity water at the Slope Water-Gulf Stream Boundary. J Geophys Res 82(24):3481–3486. doi:10.1029/JC082i024p03481

Lee TN, Williams E, Wang REJ, Atkinson L (1989) Response of South Carolina continental shelf waters to wind and Gulf Stream forcing during winter of 1986. J Geophys Res 94:10, 715–10,754

Lee TN, Yoder JA, Atkinson LP (1991) Gulf Stream frontal eddy influence on productivity of the Southeast U.S. Continental Shelf. J Geophys Res 96(C12):22,191–22,205

Lentz SJ (2003) A climatology of salty intrusions over the continental shelf from Georges Bank to Cape Hatteras. J Geophys Res 108(C10):3326. doi:10.1029/2003JC001859

Lentz SJ (2008) Observations and a model of the mean circulation over the Middle Atlantic Bight Continental Shelf. J Phys Oceanogr 38: 1203–1221

Lentz S, Guza RT, Elgar S, Feddersen F, Herbers THC (1999) Momentum balances on the North Carolina inner shelf. J Geophys Res 104(C8):18,205–18,226. doi:10.1029/1999JC900101

Lentz SJ, Carr M, Herbers THC (2001) Barotropic tides on the North Carolina shelf. J Phys Oceanogr 31:1843–1859

Li Y, Xue H, Bane JM (2002) Air-sea interactions during the passage of a winter storm over the Gulf Stream: a three-dimensional coupled atmosphere-ocean model study, J. Geophys. Res., 107(C11), 3200, doi:10.1029/2001JC001161

Luettich, R.A., Westerink, J.J., Scheffner, N.W. (1991) ADCIRC: an advanced three-dimensional circulation model for shelves, coasts and estuaries. Coast. Engrg. Res. Ct., US Army Engs. Wtrways. Experiment Station, Vicksburg, MS Report 1: Theory and Methodology of ADCIRC-2DDI and ADCIRC-3DL

MacCready P, Banas NS, Hickey BM, Dever EP, Liu Y (2009) A model study of tide- and wind-induced mixing in the Columbia River Estuary and plume. Cont Shelf Res 29:278–291

Marchesiello P, McWilliams JC, Shchepetkin A (2003) Equilibrium structure and dynamics of the California Current System J. Phys. Oceanogr 33:753–783

Mellor GL, Yamada T (1982) Development of a turbulence closure model for geophysical fluid problems. Rev Geophys 20(4):851–875. doi:10.1029/RG020i004p00851

Nelson J, He R (2012) Effect of the Gulf Stream on Winter Extratropical Cyclone Outbreaks. Atmos Res Lett 13:311–316

Nelson J, He R, Warner JC, Bane J (2014) Air-sea interactions during strong winter extratropical storms. Ocean Dyn. doi:10.1007/s10236-014-0745-2

Pietrafesa LJ, Blanton JO, Wang JD, Kourafalou V, Lee TN, Bush KA (1985) The tidal regime in the South Atlantic Bight, in Oceanography of the Southeastern U. S. Continental Shelf, Coastal Estuarine Sci., vol. 2., pp. 63 – 76. In: Atkinson LP, Menzel DW, Bush KA (eds) AGU, Washington, D. C

Pietrafesa LJ, Morrison JM, McCann MP, Churchill J, Bohm E, Houghton RW (1994) Water mass linkages between the Middle and South Atlantic bights. Deep-Sea Res 41:365–389

Savidge DK (2004) Gulf Stream meander propagation past Cape Hatteras. J Phys Oceanogr 34(9):2073–2085

Savidge DK, Austin JA (2007) The Hatteras Front: August 2004 velocity and density structure. J Geophys Res 112, C07006. doi:10.1029/2006JC003933

Savidge DK, Bane JM Jr (2001) Wind and Gulf Stream influences on along-shelf transport and off-shelf export at Cape Hatteras, North Carolina. J Geophys Res 106:11,505–11,527. doi:10.1029/2000JC000574

Savidge DK, Savidge W (2014) Seasonal export of South Atlantic and Mid-Atlantic Bight Shelf Waters at Cape Hatteras, submitted to Continental Shelf Research

Savidge DK, Edwards CR, Santana M (2007) Baroclinic effects and tides on the Cape Hatteras continental shelf. J Geophys Res 112(C09016):1–16. doi:10.1029/2006JC003832

Savidge DK, Austin JA, Blanton BO (2013) Variation in the Hatteras Front density and velocity structure Part 1: high resolution transects from three seasons in 2004–2005. Cont Shelf Res CSR2683, doi:10.1016/j.csr.2012.11.005

Savidge DK, Austin JA, Blanton BO (2013) Variation in the Hatteras Front density and velocity structure Part 2: historical setting. Continental Shelf Research, CSR2684 doi:10.1016/j.csr.2012.11.006

Shchepetkin AF, McWilliams JC (2005) The Regional Ocean Modeling System: a split-explicit, free-surface, topography following coordinates ocean model. Ocean Model 9:347–404

Xue H, Pan Z, Bane JM Jr (2000) A 2D coupled atmosphere-ocean model study of air-sea interactions during a cold air outbreak over Gulf Stream. Mon Weather Rev 128:973–996

Yin J, Schlesinger ME, Stouffer RJ (2009) Model projections of rapid sea-level rise on the northeast coast of the United States. Nat Geosci 2:262–266. doi:10.1038/NGEO462

Zhang WG, Wilkin JL, Arango HG (2010) Towards building an integrated observation and modeling system in the New York Bight using variational methods, Part I: 4DVAR data assimilation. Ocean Model 35:119–133